

Disorder-induced phase transitions in three-dimensional chiral second-order topological insulatorYedi Shen,¹ Zeyu Li,¹ Qian Niu,^{1,*} and Zhenhua Qiao^{1,2,†}¹*International Centre for Quantum Design of Functional Materials, CAS Key Laboratory of Strongly-Coupled Quantum Matter Physics, and Department of Physics, University of Science and Technology of China, Hefei, Anhui 230026, China*²*Hefei National Laboratory, University of Science and Technology of China, Hefei 230088, China*

(Received 18 September 2023; accepted 12 December 2023; published 4 January 2024)

Topological insulators have been extended to higher-order versions that possess topological hinge or corner states in lower dimensions. However, their robustness against disorder is still unclear. Here, we theoretically investigate the phase transitions of a three-dimensional chiral second-order topological insulator in the presence of disorder. Our results show that, by increasing disorder strength, the nonzero densities of states of the side surface and bulk emerge at disorder strengths of W_S and W_B , respectively. The spectral function indicates that the bulk gap is only closed at one of the $R_{4z}\mathcal{T}$ -invariant points, i.e., Γ_3 . The closing of the side surface gap or bulk gap is ascribed to a significant decrease of the elastic mean free time of quasiparticles. Based on the scaling theory of localization length, we obtain two fixed points as two critical disorder strengths for any given Fermi energy, indicating that the three-dimensional chiral second-order topological insulator gradually enters the diffusive metallic phase and Anderson insulating phase, respectively. In the end, a global phase diagram is provided to clearly demonstrate the evolution of different phases.

DOI: [10.1103/PhysRevB.109.035303](https://doi.org/10.1103/PhysRevB.109.035303)**I. INTRODUCTION**

Higher-order topological insulators, characterized by hinge or corner states protected by various spatiotemporal symmetries [1–22], have invigorated many research fields, such as spintronics and phononics [23–29]. Although these states have been extensively observed in bosonic systems [30,31], the observations are extremely limited in electronic systems. In particular, a three-dimensional (3D) chiral second-order topological insulator (SOTI), possessing gapped bulk states, gapped side surface states, and 1D topologically protected in-gap hinge states propagating unidirectionally, has not yet been experimentally observed. Given the ubiquitous disorder in crystalline materials, it is crucial to understand their robustness against disorder [32–35]. Without spin-orbit coupling or magnetic field, a disorder-induced metal-insulator transition can occur in 3D electronic systems but not 1D and 2D [36]. Therefore, it is interesting to explore the electronic transport properties of 3D chiral SOTIs under disorder.

Based on renormalization-group calculations, it was reported that 3D chiral SOTIs are always unstable against Coulomb interaction and disorder [37], which has attracted widespread discussion [38–40]. However, some key information was missing. For example, they just considered the disorder-induced one-loop self-energy correction, and only one of the $R_{4z}\mathcal{T}$ -invariant (a combination of fourfold rotation and time-reversal symmetry) \mathbf{k} points (Γ_1) were used

to study the phase transition. Here, we reexamine their robustness against disorder by considering all the $R_{4z}\mathcal{T}$ -invariant \mathbf{k} points. We find that the bulk gap closes at Γ_3 , i.e., $(k_x, k_y, k_z) = (0, 0, \pi)$, but not Γ_1 as used in previous reports. Meanwhile, by considering multiple scattering events [41–45] that is beyond the abilities of the self-consistent Born approximation [32,33,46–48] and the renormalization-group approach [37,48], we find the renormalized parameters cannot be used as the unique criterion for a phase transition under disorder. It is necessary to consider the broadening of the energy spectrum caused by multiple scattering events.

In this paper, we systematically study the phase transitions of a 3D chiral SOTI in the presence of disorder. By investigating the density of states and the averaged inverse participation ratio, we find that the side surface gap and bulk gap successively close at disorder strengths of W_S and W_B , respectively. Based on the accurate momentum-space Lanczos method [49–51], which can rigorously treat all multiscattering events from impurities, we obtain the scaling properties of low-energy quasiparticles in a disordered 3D chiral SOTI around all four $R_{4z}\mathcal{T}$ -invariant \mathbf{k} points at the first Brillouin zone. Surprisingly, the spectral function and self-energy show that the four $R_{4z}\mathcal{T}$ -invariant \mathbf{k} points exhibit different behaviors by increasing the disorder strength (see Fig. 1), i.e., disorder only closes the local gap at Γ_3 . By employing the scaling theory of localization length [52,53], we draw a phase diagram to show the phase boundaries of disorder-induced phase transitions. One can see that the 3D chiral SOTI first enters a diffusive metallic phase when the disorder strength exceeds a critical value of W_{C1} , and then transits into the Anderson insulating phase when the disorder strength is beyond the other critical value W_{C2} .

*Corresponding author: niuqian@ustc.edu.cn

†Corresponding author: qiao@ustc.edu.cn

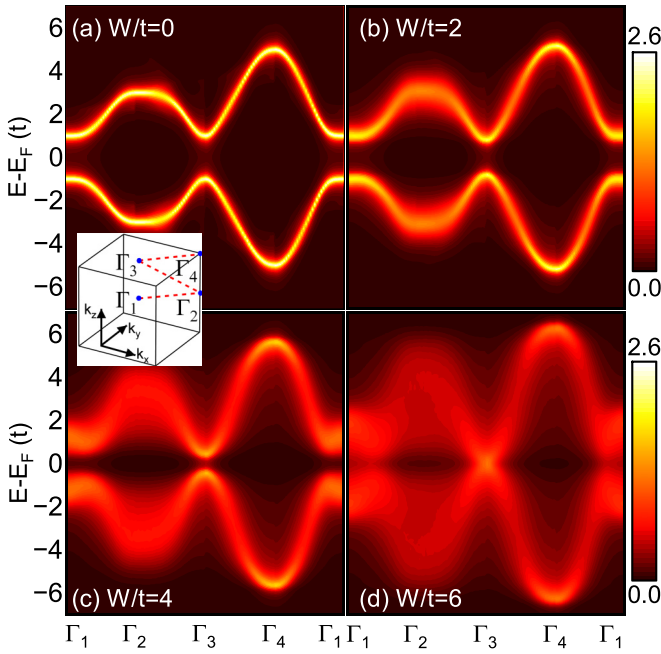


FIG. 1. Quasiparticle spectral function $A(\mathbf{k}, E)$ along high-symmetry lines consisting of four $R_{4z}\mathcal{T}$ -invariant \mathbf{k} points. The color plot is drawn in a logarithmic scale. The sample is set to be $L^3 = 160^3 a^3$. (a)–(d) Quasiparticle spectral function of s disordered 3D chiral SOTI with $W/t = 0, 2, 4,$ and 6 . Inset: Brillouin zone of the 3D chiral SOTI. Γ_{1-4} are $R_{4z}\mathcal{T}$ -invariant \mathbf{k} points.

II. 3D CHIRAL SOTI

The tight-binding model Hamiltonian of 3d chiral SOTI can be written as [23]

$$\begin{aligned}
 H_0 = & \frac{M}{2} \sum_{\mathbf{r}, \alpha} (-1)^\alpha C_{\mathbf{r}, \alpha}^\dagger \sigma_0 C_{\mathbf{r}, \alpha} \\
 & + \frac{1}{2} \sum_{\mathbf{r}, \alpha} \sum_{i=x, y, z} t_i (-1)^\alpha C_{\mathbf{r}+\hat{e}_i, \alpha}^\dagger \sigma_0 C_{\mathbf{r}, \alpha} \\
 & + \frac{\Delta_1}{2i} \sum_{\mathbf{r}, \alpha} \sum_{i=x, y, z} C_{\mathbf{r}+\hat{e}_i, \alpha+1}^\dagger \sigma_i C_{\mathbf{r}, \alpha} \\
 & + \frac{\Delta_2}{2i} \sum_{\mathbf{r}, \alpha} \sum_{i=x, y, z} (-1)^\alpha n_i C_{\mathbf{r}+\hat{e}_i, \alpha+1}^\dagger \sigma_0 C_{\mathbf{r}, \alpha}, \quad (1)
 \end{aligned}$$

where M is the mass term. t_i , Δ_1 , and Δ_2 are the nearest-neighbor hopping parameters. α (0 or 1) represents the orbital subspace, $\hat{n} = (1, -1, 0)$, and $C_{\mathbf{r}, \alpha}^\dagger$ ($C_{\mathbf{r}, \alpha}$) is the creation (annihilation) operator with spin s (\uparrow or \downarrow) at site \mathbf{r} . σ_0 and σ_i ($i = x, y, z$) are Pauli matrices for spin degrees of freedom. The basis vectors are spanned by \hat{e}_i ($i = x, y, z$). Δ_2 breaks both time-reversal symmetry $\mathcal{T} = \tau_0 \sigma_y \mathcal{K}$ and fourfold rotation symmetry $R_{4z} \equiv \tau_0 e^{-i(\pi/4)\sigma_z}$ simultaneously. For $1 < |M/t| < 3$, the system is a 3D chiral SOTI. Hereinbelow, we set $t_i = -t = -1$, $M/t = 2$, $\Delta_1/t = 1$, and $\Delta_2/t = 1$ [20].

A. Density of states and spectral function

First, we study the density of states (DOS) of a 3D chiral SOTI in the presence of disorder, which is considered as $V_{\text{dis}} = V(\mathbf{r})I_{4 \times 4}$. $V(\mathbf{r})$ is uniformly distributed between

$-W/2$ and $W/2$, where W represents the disorder strength. The $R_{4z}\mathcal{T}$ symmetry is preserved under disorder [37]. The chiral hinge states are located in the bulk and side surface gaps. It means that the occurrence of a phase transition will be related to both magnitudes of the bulk gap and the side surface gap. Therefore, the evolution of the local DOS of the side surface and bulk can characterize the robustness of hinge states against disorder. The local DOS can be evaluated as $\rho(\mathbf{r}_i, E) = -\text{Im}\langle i | \frac{1}{E-H+i\eta} | i \rangle / \pi$. Here, a small artificial broadening parameter of $\eta = 0.01t$ is adopted. Based on the well-developed Lanczos recursive method [54,55], the local DOS can be numerically calculated. To obtain a high-energy resolution and reduce the finite-size effect, a large sample of ($L^3 = 160^3 a^3$) with open boundary conditions is considered [see Fig. 2(a)]. Figure 2(b) displays the bulk DOS as a function of energy $E - E_F(t)$ for different disorder strengths, i.e., $W/t = 0, 1, 2, 3, 4, 5,$ and 6 . A pristine 3D chiral SOTI has a wide bulk gap determined by Δ_1 . With the increase of W , the side surface gap gradually decreases and remains open until the disorder strength reaches $W_S/t \approx 3.5$. Once the disorder strength exceeds W_S , a nonzero side surface DOS emerges at the Fermi level E_F , implying the closing of the side surface gap. Moreover, the bulk DOS exhibits similar behavior [see Fig. 2(c)], because the bulk gap is larger than the side surface gap, and it was closed at a stronger disorder strength of $W_B/t \approx 4.5$. The bulk and side surface DOS at E_F as a function of $W(t)$ are displayed in Fig. 2(d).

The closings of the side surface gap and bulk gap signify the phase transitions in the presence of disorder. To confirm the possible phase transitions, we elaborate on the averaged inverse participation ratio expressed as [56,57]

$$P_{\text{avg}} = \left\langle \frac{[\sum_{i, \alpha, s} |\psi_{\alpha, s}(\mathbf{r}_i)|^2]^2}{\sum_{i, \alpha, s} |\psi_{\alpha, s}(\mathbf{r}_i)|^4} \right\rangle, \quad (2)$$

where $\langle \dots \rangle$ denotes the disorder average. Figure 2(e) plots the averaged inverse participation ratio as a function of W at $E = E_F$ for different volumes $L^3/a^3 = 14^3, 16^3, 18^3,$ and 20^3 . It is known that $P_{\text{avg}} \sim L^d$ at a d -dimensional metallic phase, but $P_{\text{avg}} \sim \text{const}$ at the insulating phase. In the weak disorder regime, one can see that $P_{\text{avg}} \sim L$, implying that there are one-dimensional metallic chiral hinge states. With a disorder increase, the extensibility of the metallic chiral hinge states gradually becomes worse. After that, $P_{\text{avg}} \sim L^3$, implying that the massively extended bulk states have a primary impact on the averaged inverse participation ratio, i.e., the system goes into a diffusive metallic phase. For even larger disorder strength, $P_{\text{avg}} \sim \text{const}$, corresponding to the Anderson insulating phase. It is noteworthy that there is no 3D first-order topological insulator with a large averaged inverse participation ratio with $P_{\text{avg}} \sim L^2$.

To further illustrate the disorder effect, the properties of a quasiparticle in momentum space are studied. The low-energy effective model Hamiltonian of the 3D chiral SOTI can be expressed as [23,37]

$$\begin{aligned}
 H_0(\mathbf{k}) = & \left[M + \sum_i t_i \cos(ak_i) \right] \tau_z \sigma_0 + \Delta_1 \sum_i \sin(ak_i) \\
 & \times \tau_x \sigma_i + \Delta_2 [\cos(ak_x) - \cos(ak_y)] \tau_y \sigma_0, \quad (3)
 \end{aligned}$$

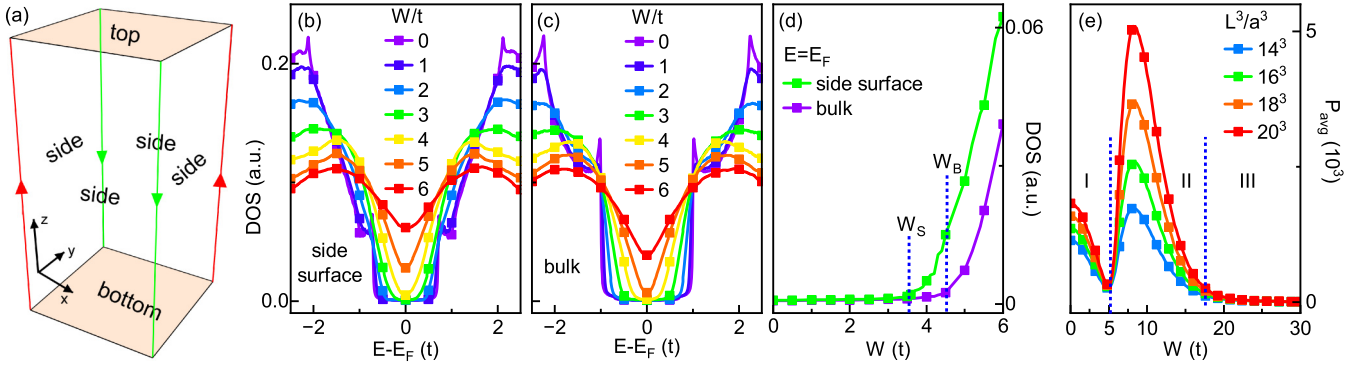


FIG. 2. (a) Schematic of a 3D chiral SOTI with open boundary conditions. (b), (c) Side surface and bulk density of states for a disordered 3D chiral SOTI with $W/t = 0, 1, 2, 3, 4, 5,$ and 6 , at a fixed system of $L^3 = 160^3 a^3$. (d) The density of states at $E = E_F$ varies with disorder strength. With an increase of disorder strength, the widths of the side surface gap and the bulk gap gradually decrease, and finally close at $W_S/t \approx 3.5$ and $W_B/t \approx 4.5$, respectively. (e) The averaged inverse participation ratio as a function of disorder strength W for different sample sizes $L^3/a^3 = 14^3, 16^3, 18^3,$ and 20^3 with open boundary conditions at $E = E_F$. P_{avg} is proportional to $L/L^3/\text{constant}$ in region I/II/III, respectively. Over 1000 ensembles are collected for each point.

where σ_i and τ_i ($i = x, y, z$) are Pauli matrices for spin and orbital degrees of freedom, respectively. a is the lattice constant. The combination of R_{4z} and \mathcal{T} is preserved and generates four $R_{4z}\mathcal{T}$ -invariant \mathbf{k} points at Γ_i , where Γ_{1-4} are $\{(0, 0, 0), (\pi, \pi, 0), (0, 0, \pi), (\pi, \pi, \pi)\}$, respectively. For the valence and conduction bands, the eigenvalues of $H_0(\mathbf{k})$ are $E_0(\Gamma_1) = \pm 1$, $E_0(\Gamma_2) = \pm 3$, $E_0(\Gamma_3) = \pm 1$, and $E_0(\Gamma_4) = \pm 5$, where \pm represents different orbitals. Each band has two spins, resulting in a twofold degeneracy. In a large 3D sample with millions of atoms ($L^3 = 160^3 a^3$), we analyze the modification of the energy spectra in momentum space based on the accurate momentum-space Lanczos recursive method [49–51], which can capture all multiscattering events. The quasiparticle spectral function is bridged with the Green's function through the equation $A(\mathbf{k}, E) = -\text{Im} G(\mathbf{k}, E)/\pi$ [50]. The energy spectra along high-symmetry lines, consisting of four $R_{4z}\mathcal{T}$ -invariant \mathbf{k} points, are displayed in Fig. 1. When $W/t = 0$, the spectral function $A_0(\mathbf{k}, E)$ is a δ function, suggesting that the wave vector \mathbf{k} is a good quantum number and all its weight is concentrated at the energy $E = E_{\mathbf{k}}$ [see Fig. 1(a)]. In the presence of disorder, the δ peak becomes broadened due to the disorder-scattering effect, giving a finite elastic mean free time to the quasiparticle, and the bulk gap begins to gradually decrease [see Figs. 1(a) and 1(b)]. The peak width is determined by the imaginary part of the self-energy, $\text{Im} \Sigma(E)$. After entering a strong scattering region, the spread of the spectral function becomes prominent, and the bulk gap eventually closes at Γ_3 , while the others remain open, as shown in Fig. 1(d). We also find $|\langle \Gamma_3, \alpha, s | V_{\text{dis}} | \Gamma_3, \alpha, s \rangle| \gg |\langle \Gamma_1, \alpha, s | V_{\text{dis}} | \Gamma_3, \alpha, s \rangle|$, which means intravalley scattering at Γ_3 is stronger than intervalley scattering from Γ_1 to Γ_3 . So, we can only focus on Γ_3 to explore the disorder-induced phase transition in momentum space.

B. Accurate self-energy of disordered 3D chiral SOTI

By utilizing the accurate momentum-space Lanczos recursive method, the phase transition can be further understood through the accurate self-energy solved by

the Dyson equation $\Sigma(\mathbf{k}, E) = G_0^{-1}(\mathbf{k}, E) - G^{-1}(\mathbf{k}, E)$. Figure 3(a) plots the real part of the quasiparticle self-energy of the valence band at Γ_1 for different disorder strengths. Due to disorder effects, the roots of $E - E_F - E_0(\mathbf{k}) = \text{Re} \Sigma(E - E_F)$ correspond to the quasiparticle dispersion $E_{\mathbf{k}}$, implying a decrease in the energy of quasiparticles. Furthermore, the elastic mean free time is inversely proportional to the imaginary part of the self-energy, given by $\tau = [\hbar / -2 \text{Im} \Sigma(E - E_F)]$, which can be used to describe the decay time of quasiparticles.

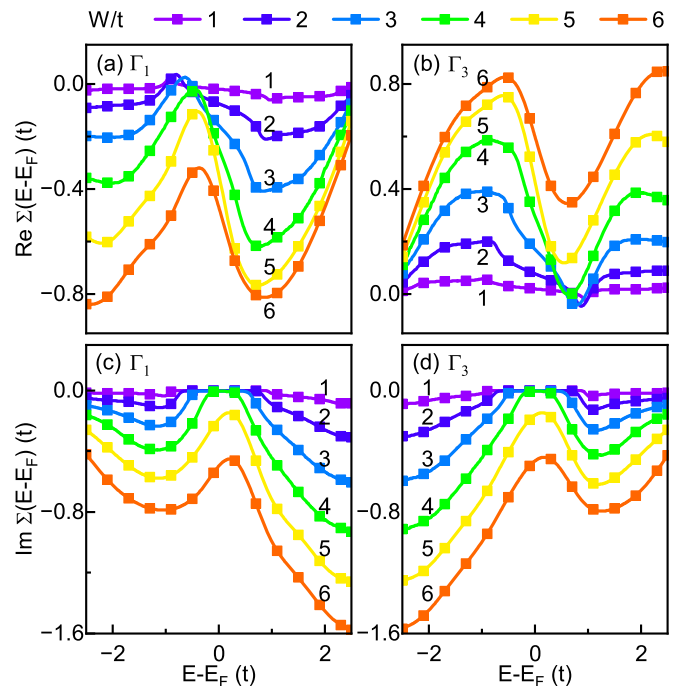


FIG. 3. (a), (b) Real and (c), (d) imaginary parts of self-energy as a function of energy for different disorder strengths ($1 \leq W/t \leq 6$) of the valence band at Γ_1 and Γ_3 , respectively. At Γ_1/Γ_3 , with the increase of disorder strength, the conduction and valence bands move away/closer from/to the Fermi level.

As shown in Fig. 3(c), the elastic mean free time at Γ_1 gradually decreases with the increase of disorder strength. Because of the particle-hole symmetry, the self-energy obtained based on the eigenstate basis satisfies the following relations, $\text{Re } \Sigma(\Gamma_1, E, \alpha_i, s) = -\text{Re } \Sigma(\Gamma_1, -E, \alpha_j, s)$ and $\text{Im } \Sigma(\Gamma_1, E, \alpha_i, s) = \text{Im } \Sigma(\Gamma_1, -E, \alpha_j, s)$ ($i \neq j$), which ensure that the dispersion relations are symmetric with respect to the Fermi level. And we find that $\text{Re } \Sigma(\Gamma_1, E, \alpha_i, s) = -\text{Re } \Sigma(\Gamma_3, -E, \alpha_j, s)$ and $\text{Im } \Sigma(\Gamma_1, E, \alpha_i, s) = \text{Im } \Sigma(\Gamma_3, -E, \alpha_j, s)$ ($i = j$), as shown in Figs. 3(b) and 3(d). From a similar analysis, we find that the energy of the quasiparticle at Γ_3 increases, and the elastic mean free time decreases with an increase of disorder strength.

Furthermore, we also explore the correction to the hopping parameters induced by disorder. By doing a unitary transformation, we transform the self-energy from the eigenstate basis to the orbital-spin basis. Then, we can construct an effective Hamiltonian including disorder, i.e., $H_{\text{eff}} = H_0(\mathbf{k}) + U_{\mathbf{k}} \Sigma(\mathbf{k}, E) U_{\mathbf{k}}^\dagger$. Due to multiple scattering events, the small elastic mean free time effectively broadens the spectral function. Therefore the corrected Δ_1 and Δ_2 are nonvanishing, the bulk gap and side surface gap become closed (see Appendix A). As functions of the running scale parameter, the renormalized Δ_1 and Δ_2 go to zero [37], but they cannot be used as a unique criterion for the phase transition in the presence of disorder. The broadening of the energy spectrum eventually leads to bulk gap closing.

III. PHASE TRANSITIONS

To precisely determine the phase boundaries, we numerically calculate the localization length ξ on a quasi-two-dimensional slice of essentially infinite length (1×10^6) and finite area L^2 by using the transfer-matrix method (see Appendix B). The periodic condition is applied to eliminate the possible hinge-state transport. We plot the normalized localization length ξ/L as a function of W at $E = E_F$ for different areas $L^2/a^2 = 6^2, 8^2, 10^2$, and 12^2 [see Fig. 4(a)]. One can find that there are two fixed points, $W_{C1}/t \approx 5.8$ and $W_{C2}/t \approx 21.6$. When $W < W_{C1}$, ξ/L decreases with an increase of L^2 , indicating that ξ/L converges to zero when $L^2 \rightarrow \infty$, signaling a localized insulating phase, i.e., the 3D chiral SOTI. When $W_{C1} < W < W_{C2}$, ξ/L enlarges with an increase of L , indicating that ξ/L diverges when $L^2 \rightarrow \infty$, signaling a delocalized metallic phase. When $W > W_{C2}$, ξ/L behaves similarly to that in the weak disorder case, meaning that it enters an Anderson insulating phase. Therefore, the fixed points W_{C1} and W_{C2} are two critical disorder strengths for the insulator-metal and metal-insulator phase transitions, respectively. To build the phase diagram in the $(E - E_F, W)$ plane, we calculate the critical disorder strengths W_{C1} and W_{C2} for different energies, which define the phase boundaries [see Fig. 4(b)].

IV. CONCLUSION

Based on accurate numerical calculation methods, we systematically analyze the disorder-driven phase transitions of the 3D chiral SOTI in the presence of disorder. The DOS and spectral function indicate that the side surface gap and bulk

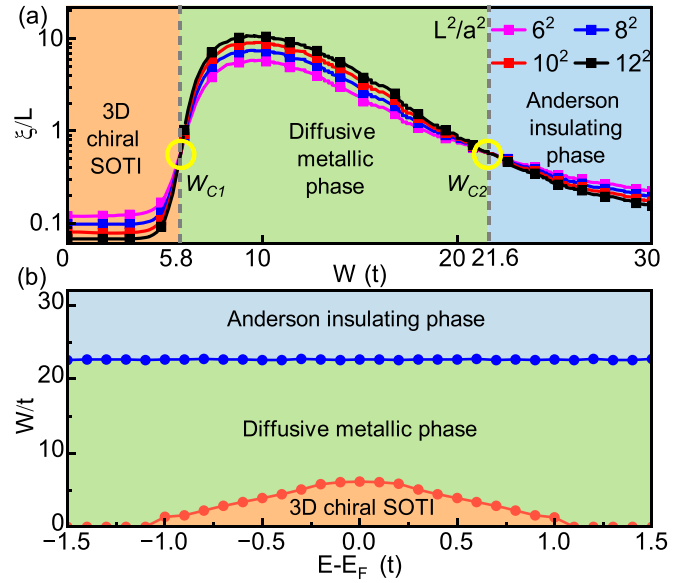


FIG. 4. (a) Normalized localization length ξ/L as a function of disorder strength W at $E = E_F$ calculated on quasi-two-dimensional slices, with a length of 1×10^6 and different areas of $L^2/a^2 = 6^2, 8^2, 10^2$, and 12^2 . $W_{C1}/t \approx 5.8$ and $W_{C2}/t \approx 21.6$ are two critical points. (b) Phase diagram in the $(E - E_F, W)$ plane.

gap successively close at disorder strengths of $W_S/t = 3.5$ and $W_B/t = 4.5$, respectively. It is noted that the bulk gap is only closed at one of the $R_{4z}\mathcal{T}$ -invariant \mathbf{k} points, i.e., Γ_3 . We also obtain the accurate self-energy to build an effective Hamiltonian, revealing that the close of the bulk gap ascribes to the reduced elastic mean free time of quasiparticles, which leads to a broadening of the spectral function. When the disorder strength is beyond W_{C1} and W_{C2} , the 3D chiral SOTI can be successively driven into two different phases: a diffusive metallic phase and an Anderson insulating phase, respectively. Our results provide a clear picture to distinguish the disorder-driven phase transitions of a 3D chiral SOTI.

ACKNOWLEDGMENTS

This work was financially supported by the National Natural Science Foundation of China (Grants No. 11974327 and No. 12004369), Innovation Program for Quantum Science and Technology (2021ZD0302800), China Postdoctoral Science Foundation (2023M733411 and 2023TQ0347), and Anhui Initiative in Quantum Information Technologies (Grant No. AHY170000). Q. Niu is supported by the National Natural Science Foundation of China (12234017). We also thank for the high-performance supercomputing services provided by the Supercomputing Center of University of Science and Technology of China.

APPENDIX A: RENORMALIZED PARAMETERS INDUCED BY DISORDER

The relationship between renormalized hopping and other energy parameters at Γ_1 and Γ_3 with the disorder strength is shown in Table I.

TABLE I. The relationship between renormalized parameters at Γ_1 and Γ_3 with the disorder strength. M_1 and M_2 are the mass terms of two orbitals, respectively.

	M_1	M_2	Δ_1	Δ_2	t_i
$W/t = 0$	2	2	1	1	-1
$W/t = 1$	1.98	1.98	1.02	1.02	-1
$W/t = 2$	1.93	1.93	1.07	1.07	-1
$W/t = 3$	1.84	1.84	1.16	1.16	-1
$W/t = 4$	1.75	1.75	1.25	1.25	-1
$W/t = 5$	$1.73 - 0.1i$	$1.73 + 0.1i$	1.27	1.27	-1
$W/t = 6$	$1.61 - 0.48i$	$1.61 + 0.48i$	1.39	1.39	-1
	M_1	M_2	Δ_1	Δ_2	t_i
$W/t = 0$	2	2	1	1	-1
$W/t = 1$	1.98	1.98	0.98	0.98	-1
$W/t = 2$	1.92	1.92	0.92	0.92	-1
$W/t = 3$	1.83	1.83	0.83	0.83	-1
$W/t = 4$	1.70	1.70	0.70	0.70	-1
$W/t = 5$	$1.51 - 0.1i$	$1.51 + 0.1i$	0.51	0.51	-1
$W/t = 6$	$1.38 - 0.44i$	$1.38 + 0.44i$	0.38	0.38	-1

APPENDIX B: THE TRANSFER-MATRIX METHOD

The localization length ξ describes the exponential decay of the transmission probability $t(E; \mathbf{x}, \mathbf{x}')$ of an electron

between two sites \mathbf{x} and \mathbf{x}' in an infinite d -dimensional system [52,53],

$$\frac{2}{\xi} = - \lim_{|\mathbf{x}-\mathbf{x}'| \rightarrow \infty} \frac{\langle \ln t(E; \mathbf{x}, \mathbf{x}') \rangle}{|\mathbf{x} - \mathbf{x}'|}. \quad (\text{B1})$$

It can be obtained by using an iterative expression expressed as

$$\begin{pmatrix} \Psi_{n+1} \\ \Psi_n \end{pmatrix} = T_n \begin{pmatrix} \Psi_n \\ \Psi_{n-1} \end{pmatrix}, \quad (\text{B2})$$

where

$$T_n = \begin{pmatrix} [t_{n+1}^{\parallel}]^{-1} (E - \varepsilon_n - H_{\perp}) & -[t_{n+1}^{\parallel}]^{-1} t_n^{\parallel} \\ 1 & 0 \end{pmatrix}$$

is the transfer matrix, Ψ_n is the wave function at all sites of the n slice, ε_n is the energy, H_{\perp} is the hopping Hamiltonian in the n th slice, and t_{n+1}^{\parallel} is the diagonal matrix representing the hopping elements connecting the $n-1$ slice with the n slice. The evolution of the wave function is given by the product of the transfer matrices $\tau_k = T_k \times T_{k-1} \times \dots \times T_1$. The eigenvalues of $\lim_{k \rightarrow \infty} (\tau_k^t \times \tau_k)^{1/2k}$ exist and the smallest Lyapunov exponent corresponds to the largest localization length ξ .

- [1] L. Fu, C. L. Kane, and E. J. Mele, *Phys. Rev. Lett.* **98**, 106803 (2007).
- [2] L. Fu and C. L. Kane, *Phys. Rev. B* **76**, 045302 (2007).
- [3] Y. B. Yang, Kai Li, L. M. Duan, and Y. Xu, *Phys. Rev. B* **103**, 085408 (2021).
- [4] H. Araki, T. Mizoguchi, and Y. Hatsugai, *Phys. Rev. B* **99**, 085406 (2019).
- [5] W. A. Benalcazar, B. A. Bernevig, and T. L. Hughes, *Phys. Rev. B* **96**, 245115 (2017).
- [6] Z. Song, Z. Fang, and C. Fang, *Phys. Rev. Lett.* **119**, 246402 (2017).
- [7] M. Sitte, A. Rosch, E. Altman, and L. Fritz, *Phys. Rev. Lett.* **108**, 126807 (2012).
- [8] F. Zhang, C. L. Kane, and E. J. Mele, *Phys. Rev. Lett.* **110**, 046404 (2013).
- [9] F. Liu, *Coshare Science* **01**, v3, 1 (2023).
- [10] M. Ezawa, *Phys. Rev. B* **97**, 155305 (2018).
- [11] J. Ahn and B. J. Yang, *Phys. Rev. B* **99**, 235125 (2019).
- [12] Z. Wang, B. J. Wieder, J. Li, B. Yan, and B. A. Bernevig, *Phys. Rev. Lett.* **123**, 186401 (2019).
- [13] M. Lin and T. L. Hughes, *Phys. Rev. B* **98**, 241103(R) (2018).
- [14] S. H. Kooi, G. van Miert, and C. Ortix, *Phys. Rev. B* **98**, 245102 (2018).
- [15] G. van Miert and C. Ortix, *Phys. Rev. B* **98**, 081110(R) (2018).
- [16] S. Franca, J. van den Brink, and I. C. Fulga, *Phys. Rev. B* **98**, 201114(R) (2018).
- [17] A. Matsugatani and H. Watanabe, *Phys. Rev. B* **98**, 205129 (2018).
- [18] F. Schindler, Z. Wang, M. G. Vergniory, A. M. Cook, A. Murani, S. Sengupta, A. Y. Kasumov, R. Deblock, S. Jeon, I. Drozdov *et al.*, *Nat. Phys.* **14**, 918 (2018).
- [19] S. A. A. Ghorashi, T. L. Hughes, and E. Rossi, *Phys. Rev. Lett.* **125**, 037001 (2020).
- [20] C. A. Li, S. B. Zhang, J. Li, and B. Trauzettel, *Phys. Rev. Lett.* **127**, 026803 (2021).
- [21] A. K. Ghosh, T. Nag, and A. Saha, *Phys. Rev. B* **104**, 134508 (2021).
- [22] S. Saha, T. Nag, and S. Mandal, *Europhys. Lett.* **142**, 56002 (2023).
- [23] F. Schindler, A. M. Cook, M. G. Vergniory, Z. Wang, S. S. P. Parkin, B. A. Bernevig, and T. Neupert, *Sci. Adv.* **4**, eaat0346 (2018).
- [24] O. Pozo, C. Repellin, and A. G. Grushin, *Phys. Rev. Lett.* **123**, 247401 (2019).
- [25] B. Fu, Z. A. Hu, and S. Q. Shen, *Phys. Rev. Res.* **3**, 033177 (2021).
- [26] S. Komori and K. Kondo, *J. Phys. Commun.* **4**, 125005 (2020).
- [27] H. Li and K. Sun, *Phys. Rev. Lett.* **124**, 036401 (2020).
- [28] A. Dutt, M. Minkov, I. A. D. Williamson, and S. Fan, *Light: Sci. Appl.* **9**, 131 (2020).
- [29] Y. Yang, J. Lu, M. Yan, X. Huang, W. Y. Deng, and Z. Y. Liu, *Phys. Rev. Lett.* **126**, 156801 (2021).
- [30] Y. You, T. Devakul, F. J. Burnell, and T. Neupert, *Phys. Rev. B* **98**, 235102 (2018).

- [31] O. Dubinkin and T. L. Hughes, *Phys. Rev. B* **99**, 235132 (2019).
- [32] C. Wang and X. R. Wang, *Phys. Rev. Res.* **2**, 033521 (2020).
- [33] C. Wang and X. R. Wang, *Phys. Rev. B* **103**, 115118 (2021).
- [34] J. H. Wang, Y. B. Yang, N. Dai, and Y. Xu, *Phys. Rev. Lett.* **126**, 206404 (2021).
- [35] A. L. Szabó and B. Roy, *Phys. Rev. Res.* **2**, 043197 (2020).
- [36] E. Abrahams, P. W. Anderson, D. C. Licciardello, and T. V. Ramakrishnan, *Phys. Rev. Lett.* **42**, 673 (1979).
- [37] P. L. Zhao, X. B. Qiang, H. Z. Lu, and X. C. Xie, *Phys. Rev. Lett.* **127**, 176601 (2021).
- [38] H. Q. Li, H. Y. Kee, and Y. B. Kim, *Phys. Rev. B* **106**, 155116 (2022).
- [39] Y. W. Lee and M. F. Yang, *Phys. Rev. Lett.* **130**, 219701 (2023).
- [40] J. R. Wang and C. J. Zhang, *arXiv:2202.03417*.
- [41] E. V. Castro, M. P. López-Sancho, and M. A. H. Vozmediano, *Phys. Rev. B* **92**, 085410 (2015).
- [42] Z. Qiao, Y. Han, L. Zhang, K. Wang, X. Deng, H. Jiang, S. A. Yang, J. Wang, and Q. Niu, *Phys. Rev. Lett.* **117**, 056802 (2016).
- [43] Y. Kuno, *Phys. Rev. B* **100**, 054108 (2019).
- [44] S. S. Krishtopenko, M. Antezza, and F. Teppe, *Phys. Rev. B* **101**, 205424 (2020).
- [45] U. Chattopadhyay, S. Mittal, M. Hafezi, and Y. D. Chong, *Phys. Rev. B* **103**, 214201 (2021).
- [46] Y. Zheng and T. Ando, *Phys. Rev. B* **65**, 245420 (2002).
- [47] C. A. Li, B. Fu, Z. A. Hu, J. Li, and S. Q. Shen, *Phys. Rev. Lett.* **125**, 166801 (2020).
- [48] P. M. Ostrovsky, I. V. Gornyi, and A. D. Mirlin, *Phys. Rev. B* **74**, 235443 (2006).
- [49] W. Zhu, Q. W. Shi, X. R. Wang, X. P. Wang, J. L. Yang, J. Chen, and J. G. Hou, *Phys. Rev. B* **82**, 153405 (2010).
- [50] W. Zhu, W. Li, Q. W. Shi, X. R. Wang, X. P. Wang, J. L. Yang, and J. G. Hou, *Phys. Rev. B* **85**, 073407 (2012).
- [51] B. Fu, W. Zhu, Q. W. Shi, Q. X. Li, J. L. Yang, and Z. Y. Zhang, *Phys. Rev. Lett.* **118**, 146401 (2017).
- [52] A. MacKinnon and B. Kramer, *Phys. Rev. Lett.* **47**, 1546 (1981).
- [53] L. Sheng, D. Y. Xing, D. N. Sheng, and C. S. Ting, *Phys. Rev. B* **56**, R7053 (1997).
- [54] S. Wu, L. Jing, Q. Li, Q. W. Shi, J. Chen, H. Su, X. Wang, and J. Yang, *Phys. Rev. B* **77**, 195411 (2008).
- [55] W. Zhu, Q. W. Shi, X. R. Wang, J. Chen, J. L. Yang, and J. G. Hou, *Phys. Rev. Lett.* **102**, 056803 (2009).
- [56] J. H. Pixley, P. Goswami, and S. Das Sarma, *Phys. Rev. Lett.* **115**, 076601 (2015).
- [57] H. Li, C. Z. Chen, H. Jiang, and X. C. Xie, *Phys. Rev. Lett.* **127**, 236402 (2021).